Caging and excited state emission of ICN trapped in cryogenic matrices: experiment and theory†

Jan Helbing,[a] Majed Chergui,*[a] Sebastian Fernandez-Alberti,[b] Julian Echave,[b] Nadine Halberstadt[c] and J. Alberto Beswick[c]

[a] Institut de Physique de la Matière Condensée, BSP, Université de Lausanne, CH-1015 Lausanne-Dorigny, Switzerland
[b] CEI, Universidad Nacional de Quilmes, 1876 Bernal, Argentina
[c] IRSAMC, Université Paul Sabatier, 31062 Toulouse, France

We discuss the cage induced stabilisation of fragments in excited electronic states following the UV-dissociation of ICN in cryogenic matrices. Emission spectra recorded upon Ã-band excitation of ICN in solid neon, argon and krypton exhibit a long progression of broad bands due to a weakly bound electronically excited state, presumably one of the low-lying triplet states $^3\Pi_1$ or $^3\Pi_2$ of ICN. A lifetime analysis favours the $^3\Pi_2$ state. Molecular dynamics with quantum transitions (MDQT) simulations were conducted on six coupled electronic potential energy surfaces in a matrix of 498 argon atoms. Although a complete potential energy surface for the $^3\Pi_2$ state is not available, it is known to be very similar to the $^3\Pi_1$ one. Therefore only the 6 available [$^3\Pi_1$ (A′, A″), $^3\Pi_{0^+}$, $^1\Pi_1$ (A′, A″), X $^1\Sigma^+$] *ab initio* electronic potential energy surfaces were considered. The results predict a 2% probability of stabilisation in the shallow minimum of the triplet excited state. The molecule adopts a linear ICN configuration with a mean value of the I–CN distance far away from the absorption Franck–Condon region. The simulations also deliver insight into the mechanism of cage-induced population trapping in excited state surfaces, which is not accessible in the gas phase.

I. Introduction

Compared to the gas phase even the simplest photochemical reaction, *e.g.* unimolecular dissociation, becomes a complex problem in the condensed phase. The presence of a solvent cage induces several new processes: it may completely hinder the permanent separation of fragments by exerting a steric hindrance (the so-called cage effect), or substantially reduce the quantum efficiency for permanent dissociation. The caged fragments may recombine and get trapped in an electronically excited state or directly relax in the electronic ground state.[1,2] In the case of triatomic or larger molecules the fragments may recombine in a configuration different from the parent species, giving rise to cage induced isomerization.[3] Over the past ten years there has been a systematic attempt to describe all these processes in detail using model systems consisting of rare gas solids or clusters doped with molecular impurities. The process of cage exit of fragments has been intensively studied on H_2O, H_2S, HCl, and halogens trapped in rare gas matrices by groups in Berlin and Irvine.[1,2,4–10] The caging of fragments has been investigated on a femtosecond timescale by the Zewail group for I_2 in Ar clusters[11] and by Apkarian and co-workers in the case of matrix isolated I_2.[9,10] The subsequent relaxation of the recombining molecule on the ground state surface, which has been investigated by Harris and co-workers for I_2 in liquid solvents,[12] is of much longer duration.

The stabilisation of fragments on excited state surfaces is a less studied, yet not less frequent process, probably because depopulation mechanisms often make their observation difficult. Such stabilisation may occur even on surfaces that are repulsive for the free molecule by conversion into 'bound'

states due to the effect of the cage. An example is the ICF_3 molecule for which the I and CF_3 fragments are trapped at large internuclear separation in a shallow potential well, which is not accessible by the gas phase, but can be populated in the matrix due to the repulsive wall induced by the surrounding atoms.[13] Similar examples were reported for ICH_3 and ICD_3 in rare gas solids.[14] More recently the caging of spin-orbit excited $I^*(^2P_{1/2}) + I^*(^2P_{1/2})$ atom pairs in liquids and cryogenic matrices has also been observed.[15] Fragment stabilisation in matrices on surfaces with a very shallow potential minimum far from the absorption Franck–Condon window is interesting from a spectroscopic point of view, since the bound part of these surfaces cannot be accessed in the gas phase. Furthermore, if stabilisation occurs at large internuclear distances on potentials correlating to the ground state asymptote, solvent induced non-adiabatic couplings near the asymptotic dissociation limit can be studied. This problem is a central issue in condensed phase chemical dynamics and has received renewed interest, especially from theoreticians, due to the development of more powerful computing techniques.[16–21]

In this paper we address the issue of the trapping of fragments in shallow or repulsive potentials by cage effects in the case of the ICN molecule in rare gas matrices. The observation of fragments trapped in excited states is analysed in detail by molecular dynamics simulations and discussed in the light of non-adiabatic effects in the recombination process.

II. Experimental

Commercially available ICN (purity 95–97%, Aldrich) was used after purification by sublimation. Its vapour at room temperature (vapour pressure *ca.* 1 mbar) was premixed with Ne (4.8), Ar (6.0) or Kr (5.0) at ratios of typically 1 : 1000 and

---

co-condensed onto a LiF window cooled to temperatures between 4 and 40 K by a liquid He flow cryostat in an UHV chamber (background pressure $< 10^{-9}$ mbar). The sample growth was controlled by monitoring the interference pattern produced by a HeNe laser reflected off the sample. In solid Ar very high optical quality samples were obtained with growth rates of approx. 10 μm h^{-1} at 20 K, typically during 3–6 h. Neon matrices were grown at 4 K and Kr matrices at 30 K.

The samples were excited using an Excimer laser at 248 nm (KrF) or a YAG-laser pumped optical parametric oscillator, providing tuneable ns pulses between 450 and 680 nm, which were then frequency doubled.

Fluorescence light, collected at 90° with respect to the laser beam, was dispersed in either a Jobin–Yvon or an Acton Research monochromator, equipped with 300 and 150 l mm^{-1} gratings, and detected using a CCD camera or a photomultiplier. The photomultiplier signal was recorded using a 600 MHz digital oscilloscope or a photon counter for fluorescence lifetime measurements.
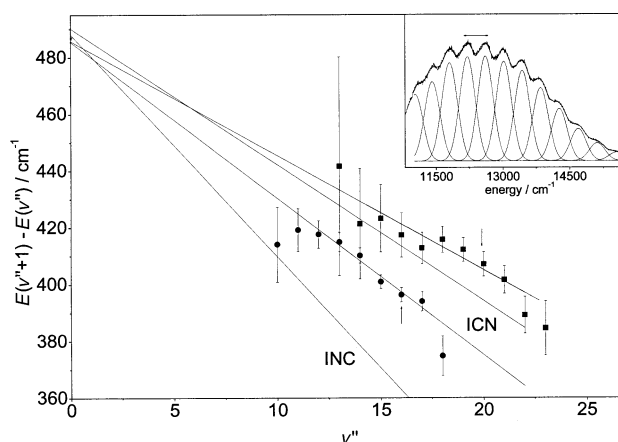
A. Results

The left-hand side of Fig. 1 shows the IR emission bands recorded upon excitation of the Ã-continuum of ICN in neon, argon and krypton matrices at 248 nm. While the emission band in neon matrices shows no structure, a well-defined vibrational progression can be seen both in solid argon and krypton. The structure is more pronounced, the lower the temperature of the sample. With respect to argon the maximum of the band is slightly blue shifted in krypton (≈ 200 cm^{-1}) and more strongly blue shifted in neon (≈ 500 cm^{-1}). The measured lifetime of this emission is 680 ± 50 μs in Ne, 320 ± 20 μs in Ar and 180 ± 20 μs in Kr matrices (right hand side of Fig. 1). In argon, where the most extensive measurements were carried out, we found no dependence of the lifetime on sample concentration (1 : 300–1 : 2000), temperature (4–30 K) and sample history (annealing, irradiation). The emission of Fig. 1 can be excited at all wavelengths between 230 and 300 nm (i.e. within the Ã-band absorption of ICN), and the emission intensity scales linearly with laser power. It is immediately present after sample growth and the observation of the near infrared bands does not depend on the purity of the ICN used for preparation. This excludes impurities [such as I_2 or $(CN)_2$] as possible emitting species. Clusters or dimers can be excluded from the observation of a broad, unstructured emission band with a sub 100 μs lifetime in large free standing crystals grown from a liquid ICN–Ar mixture, which is probably due to clusters, and which is blue shifted by approximately 500 cm^{-1} with respect to the band shown in Fig. 1b.
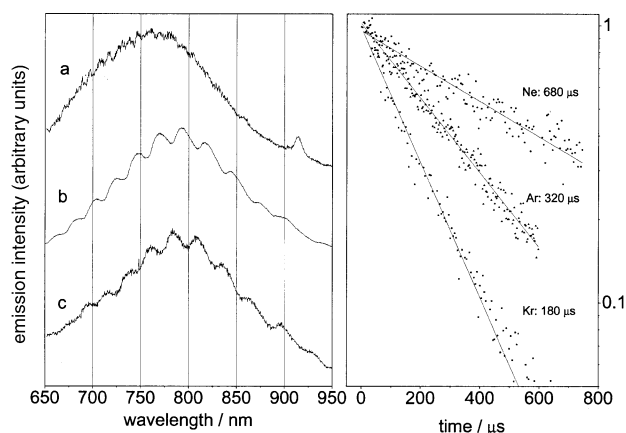
Due to the large width of the emission bands, the intensity distribution in Fig. 1 is strongly biased by the detection efficiency of our set-up. In particular, the quantum efficiency of the silicon based CCD camera rapidly drops for wavelengths longer than 800 nm. In addition, a detector which is linear in wavelength, 'stretches' the spectrum at lower energies. Taking this into account, we have attempted to correct our spectra and found that the 'true' maximum of the band in argon is located between 11 800 and 12 200 cm^{-1}.[22] The use of two different monochromators and CCD cameras in the course of this work (Jobin Yvon and Acton) as well as photomultiplier detection have, however, shown that an unambiguous intensity correction is not possible with our present setup. Furthermore the division of the spectra by the CCD response function is increasing the uncertainty in fitting the maxima of the structured emissions, which becomes larger than the anharmonicity of the bands.[22] Here we have omitted the latter correction and fitted a large set of Ar emission data, recorded with different detectors, by gaussian lineshapes of fixed width (FWHM = 410–420 cm^{-1}). Two typical results are shown in a Birge–Sponer plot in Fig. 2. The solid lines represent linear fits to the central 6 data points (smallest error) and the vibrational levels were assigned under the requirement that the data fit the ground state fundamental I–C stretch frequency of ICN in Ar (487 cm^{-1},[23] see Table 1 and discussion below). The anharmonicities obtained from these fits lie in the range of $\omega_e x_e = 2$–3 cm^{-1}, though a few data sets permit smaller or larger slopes. For krypton much fewer spectra were recorded and analysed, but an anharmonicity $\omega_e x_e$ close to 2 cm^{-1} fits the data well.

Fig. 2 Birge–Sponer plots for the near infrared emission of ICN in Ar, resulting from a fit using gaussian lineshapes of fixed width (FWHM = 410–420 cm^{-1}) as shown in the inset [$I(E)$ was obtained by dividing the wavelength spectrum by (dE/dλ)]. The solid lines represent linear fits to the central 6 datapoints with the smallest error and yield $\omega_e x_e = 2.0$ cm^{-1} and $\omega_e x_e = 2.8$ cm^{-1}, respectively. The vibrational levels were assigned under the requirement that the data fit the measured ground state fundamental I–C stretch frequency of ICN in Ar (487 cm^{-1}, ref. 26). The first and third lines from bottom correspond to ground state Morse-potentials for linear ICN and INC according to ab initio calculations[14] with $\omega_e x_e = 2.4$ cm^{-1} and $\omega_e x_e = 3.7$ cm^{-1}, respectively.

Table 1 Ground state potential parameters for linear ICN and INC

|	ICN[a]	INC[a]	ICN in Ar	ICN in Kr
D_e	25 512 cm^{-1}	15 674 cm^{-1}	—	—
$\omega_e x_e$	2.40 cm^{-1}	3.92 cm^{-1}	2–3 cm$^{-1 b}$	$\sim$2 cm$^{-1 b}$
ω_0	490.2 cm^{-1}	488.2 cm^{-1}	487 cm$^{-1 c}$	—

[a] From fit of Morse potential to ab initio data of ref. 25. [b] This work. [c] From FTIR absorption measurements.[23]

Fig. 1 Left: near infrared emission band observed under 250 nm excitation of ICN in different rare gas matrices: (a) neon, (b) argon, (c) krypton. Right: corresponding fluorescence decay curves fitted by monoexponentials.

A number of additional measurements have been carried out, that are important for the assignment of the observed emission bands. They are shortly summarised here but are presented in more detail elsewhere.[22] Most importantly, a series of photochemical processes take place upon UV-irradiation.

Upon excitation near 250 nm ICN is transformed into INC with a quantum efficiency in Ar in the range of 30–70%. The formation of INC in Ar and Kr matrices was first suggested by Haas and co-workers from FTIR absorption measurements.[23,24] Its spectroscopic signature in the UV is an absorption band centred at 245 nm and overlapping with the original ICN absorption band (Fig. 3). In the case of Ar matrices the connection between the IR and UV absorption bands was established by the very similar kinetics under irradiation.[22] In particular, the growth of both IR and UV absorption bands quickly saturates under irradiation at 250 nm, both the UV and the IR absorption bands are stable under annealing, and their formation can be completely reversed by subsequent irradiation in the 380 nm region. It can be seen in Fig. 3 that the same new UV-absorption band is also forming in Kr matrices. With respect to the initial ICN absorption, it grows stronger under UV-irradiation in krypton than in argon matrices, similar to the relative intensities observed for the IR absorption bands.[24] Due to the UV-absorption band of INC, a photostable equilibrium ICN ↔ INC is established (in Ar after a 2.6% loss of ICN[23]), since excited INC molecules can efficiently transform back to ICN upon UV-irradiation. Once equilibrium is reached the absorption at 250 nm due to INC molecules, though much fewer in number, is comparable to that of the ICN molecules, due to a much larger absorption coefficient of INC. This implies similar quantum efficiencies for the ICN* → INC and the ICN ← INC* processes in Ar. The fact that the INC equilibrium concentration upon 250 nm irradiation is higher in Kr shows that these quantum efficiencies are matrix dependent.
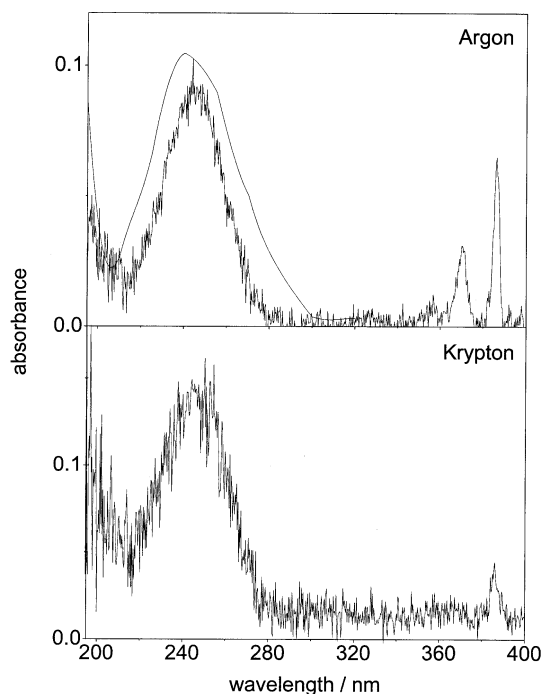
Fig. 3 Smooth line: absorption profile of ICN in solid Ar before irradiation. The Ã-band absorption is centred at 242 nm and the α-band is absorbing at wavelengths shorter than 210 nm; solid lines: UV absorption bands forming under 248 nm irradiation of ICN-doped Ar and Kr matrices. The broad feature at 245 nm is assigned to INC, while the narrow absorption band at 386 nm is due to CN fragments. These spectra were obtained using the spectrum of a sample before irradiation as reference.

Excitation of the α-band of ICN at 193 nm also leads to the near infrared emission shown in Fig. 1. Under irradiation at this wavelength 5 times more INC is formed (in Ar) than upon 248 nm irradiation.[22] Furthermore, the emission intensity in the infrared (Fig. 1) under 250 nm excitation is much stronger when a large amount of INC has previously been prepared by 193 nm irradiation. The surplus of INC with respect to the 250 nm equilibrium concentration is, however, rapidly reduced under 250 nm irradiation, as both the UV-absorption band of INC and the IR emission lose intensity.

On a longer timescale (with a quantum efficiency of ≈3% in Ar, ref. 22) the formation of CN fragments is observed upon 250 nm irradiation (Ã-band excitation of ICN) in all three matrices. At the same time the intensity of the near infrared bands of Fig. 1 is decreasing. Part of this intensity can be recovered by subsequent annealing of the sample as some of the I and CN fragments recombine (witnessed by a decrease in CN fragment absorption). During this recombination process the IR-emission, though less structured, is observed as thermofluorescence. Iodine (I_2) or CN photoproducts (or its Rg-complexes) can therefore be excluded as species responsible for the emission bands of Fig. 1, and we can limit the discussion to the ICN–INC system.

B. Assignment of the emission spectra

There is a strong decrease in near infrared emission intensity when transforming ICN into INC using 250 nm laser light. This can be observed when a large concentration of INC is previously prepared by 193 nm irradiation of the sample. The initial strength of the emission in this case is due to a 5 times stronger absorbance by INC molecules as compared to the original matrix containing only ICN,[22] which shows that the near infrared emission is observed upon excitation of INC. On the other hand, the emission cannot be due to excitation of the INC isomer alone, since it is present immediately after sample growth and the emission intensity does not change significantly on the timescale of ICN → INC conversion under 250 nm irradiation. Thus the excitation of both ICN and its isomer INC in Ar and Kr matrices at 250 nm lead to the near infrared emission.

The strongly absorbing state in the INC configuration is not part of the Ã-continuum states, and no potential energy surfaces are available at higher energies. An *ab initio* treatment including the relevant higher potentials for INC excitation at 250 nm would be very interesting, since the quantitative determination of the ICN–INC photoequilibrium concentration at this wavelength[24] provides a sensitive test for the quality of such a calculation. With only the Ã-band potentials available, here we limit ourselves to the processes after Ã-band excitation of ICN at 250 nm, which are treated by MD-simulations.

The slow fluorescence decay clearly shows that the observed near infrared emission stems from completely relaxed population in an excited electronic state, emitting to the ground state of the system. According to the *ab initio* calculations[25] the minima of the $^3\Pi_1$, $^1\Pi_1$ and $^3\Pi_{0+}$ surfaces are found in either the linear ICN or INC configuration. This is also true for the $^3\Pi_2$ excited state, which is lower in energy but largely parallel to the $^3\Pi_1$ surface.[26] These minima are found at large I–CN fragment elongations, and indeed the observed vibrational spacing of 390–430 cm^{-1} is typical of high overtones of the I–CN or I–NC stretch mode in the ground state,[23] which is the dominant reaction co-ordinate for photodissociation and recombination.

We have fitted the peak energies of the emission bands in Fig. 1 to the energy levels of one-dimensional Morse potentials for linear ICN and INC in the ground state, given by the *ab initio* calculations.[25] The parameters are given in Table 1. For ICN in Ar we find that the peak of emission at 12 200

cm^{-1} corresponds to the $v'' = 18 \pm 1$ vibrational level of the I–C stretch. This level is located about 16 800 cm^{-1} below the I(^{2}P$_{3/2}$) + CN($^2\Sigma^+$) dissociation limit. Also, according to this fit the minimum of the emitting state would be located at an I–CN distance of 3.13 ± 0.03 Å, ~5000 cm^{-1} below the first dissociation limit. A similar fit, using the ground state potential in the INC configuration, yields $v'' = 14$ for the vibrational level (I–N stretch) reached by the emission at 12 200 cm^{-1} and a minimum of the excited state of $R = 3.0$ Å (I–CN distance). This excited state minimum would be located about 2000 cm^{-1} above the I(^{2}P$_{3/2}$) + NC($^2\Sigma^+$) dissociation limit, a region where no electronic states are located according to the *ab initio* calculations (see Fig. 1). This analysis thus favours ICN rather than INC as responsible for the observed IR emission.

While confirming the assignment to ICN, an analysis purely based on experimental data in argon (Fig. 2) widens the limits that can be given for the position of the minimum of the emitting state. The experimentally determined anharmonicity of 2–3 cm^{-1} fits well the *ab initio* value of 2.4 cm^{-1} for ICN,[25] but not the 3.9 cm^{-1} for INC. The emission peak at 12 200 cm^{-1} can be assigned to a ground state vibrational level $v'' = 16$–20 of ICN, with the emitting state located 4000–6000 cm^{-1} below the dissociation limit, at an I–CN distance of 3.05–3.25 Å.

The above considerations limit the choice of emitting states to the $^3\Pi_1$ or to the $^3\Pi_2$ state of ICN, that both correlate to the I(^{2}P$_{3/2}$) + CN($^2\Sigma^+$) asymptote. Both have shallow minima of 900 cm^{-1} and 2500 cm^{-1}, respectively, at an I–CN distance near 3.4 Å.[25,26] The $^3\Pi_1$ state is responsible for the red wing in the Ã-band absorption spectrum of ICN near 280 nm with an oscillator strength of $f = 0.46 \times 10^{-3}$ for the $^3\Pi_1 \leftarrow X^1\Sigma_0^+$ transition in the Franck–Condon region.[25] The use of this value in connection with the emission at 800 nm, yields an estimate for the radiative lifetime of the $^3\Pi_1$ state of ≈ 20 μs.

The measured lifetimes are much longer in all 3 matrices studied, and in neon, which should yield the value closest to the one in the gas phase, 680 ± 50 μs are measured. It is thus very unlikely that the $^3\Pi_1 \rightarrow X^1\Sigma_0^+$ transition is responsible for the observed transition.

The $^3\Pi_2$ state, on the other hand, is the lowest lying excited state of ICN. It is not observed in absorption since the $^3\Pi_2 \leftarrow X^1\Sigma_0^+$ transition is strongly forbidden in the gas phase. In matrices, however, this transition can become weakly allowed and emission from this state may be observed, especially in the absence of efficient non-radiative relaxation channels. Energy considerations also favour the lowest lying $^3\Pi_2$ state as the state responsible for the IR emission. Given these arguments, we therefore assign the weakly structured emission band shown in Fig. 1 to the $^3\Pi_2 \rightarrow X^1\Sigma_0^+$ transition of ICN.

The assignment of the near infrared emission to caged fragments that get trapped in a shallow potential is supported by the molecular dynamics simulations which are detailed below.

III. Simulations

Molecular dynamics simulations of the photofragmentation and recombination dynamics of ICN were performed in solid argon at constant temperature. The molecular dynamics with quantum transitions (MDQT) method was used as implemented by Tully.[16,17] Briefly, the nuclei are treated classically and they evolve on a single electronic potential energy surface (PES) at a given time. Hops of the classical variables from one electronic surface to another are governed by the coefficients of the electronic wave function which is propagated quantum mechanically on the basis of the electronic states of ICN. The electronic wave packet is written as:

$$|\Psi\rangle = \sum_{i=1}^{6} c_i(t)|\phi_i\rangle \tag{1}$$

where the $|\phi_i\rangle$, $i = 1$–6 are the diabatic electronic states of ICN and $c_i(t)$ obey

$$\frac{\partial c_i}{\partial t} = -\frac{i}{\hbar} \sum_j V_{i,j}(Q(t))c_j(t) \tag{2}$$

with $V_{i,j}(Q(t))$ being the matrix elements of the electronic Hamiltonian matrix evaluated at the positions $Q(t)$ of the nuclei.

The probability for a quantum transition from the current electronic state i to all other states j is calculated at each integration step along the trajectory as

$$g_{i \rightarrow j} = \frac{\Delta t \, 2 \, \text{Im}\{c_i(t)V_{i,j}(Q(t))c_j^*(t)\}}{|c_i(t)|^2} \tag{3}$$

with the condition that if $g_{i \rightarrow j} < 0$ then $g_{i \rightarrow j} = 0$. Details about the procedure can be found elsewhere.[27]

Six coupled electronic PES were considered: ($^3\Pi_1$(A′, A″), $^3\Pi_{0+}$, $^1\Pi_1$(A′, A″), $X^1\Sigma^+$). Two of them ($^3\Pi_{0+}$ and $^1\Pi_1$) present a conical intersection at short I–CN distances that exists both in the gas phase and the condensed phase. In the latter however, the environment induces additional couplings, which are particularly efficient at large interfragment distances.

The ICN electronic PES, interstate couplings at short I–CN distances and transition moments, as well as the Ar–ICN and Ar–Ar interaction potentials used in this work were taken from Morokuma and co-workers.[25,28] Interstate couplings at large I–CN distances were obtained from a diatomic-in-molecules (DIM) treatment[18–20,29–32] of the mixing between different spin-orbit states of iodine induced by the argon atoms, with the potential parameters determined by Neumark and collaborators.[31] The procedure to obtain ICN states and couplings at large I–CN distances for the I(^{2}P$_{3/2}$) + CN($X^2\Sigma^+$) was described elsewhere.[27,32]

Trajectories were started by putting in the system an energy corresponding to a 266 nm photon excitation. This wavelength was chosen in order to facilitate comparison of simulations and time resolved experiments carried out in Lausanne. In the context of this work it is only important to note that excitation with a fs-laser at 266 nm yields emission spectra identical to those of Fig. 1 (ref. 22). The initial configurations were taken from configurations stored during a previous stabilisation simulation of 200 ps of the system in the ICN ground state with an internal energy corresponding to $T' = 49$ K (see below). To simulate the finite temporal width of the laser pulse (250 cm^{-1}) we filtered these stored configurations according to the method from ref. 21. The probability of starting from a given electronic state [$^3\Pi_1$(A′, A″), $^3\Pi_{0+}$ or $^1\Pi_1$(A′, A″)] was taken as the product of the probability deduced from these filtered configurations for that state (0.31 : 0.31 : 0.32 : 0.03 : 0.03) by the one corresponding to its relative transition intensity (0 : 03 : 0.03 : 0.66 : 0.14 : 0.14),[25] resulting in a final ratio (0.04 : 0.04 : 0.88 : 0.02 : 0.02).

It is important at this point to stress a few differences with our previous calculations.[27] In both cases, the infinite lattice of the matrix was simulated using the minimum image convention.[33] The ICN molecule was described using its Jacobi vectors $\boldsymbol{R}$, $\boldsymbol{r}$, $\boldsymbol{R}_{CM}$ in the Cartesian laboratory co-ordinate system, where $\boldsymbol{R}$ is the vector joining I and the CN centre of mass, $\boldsymbol{r}$ is the vector from C to N and $\boldsymbol{R}_{CM}$ is the centre of mass position vector. Cartesian co-ordinates were used for Ar atoms. In a previous work[27] the Ar matrix has been simulated by 254 atoms at 4 K around the (fcc) equilibrium geometry of the crystal and simulations were run for 3 ps at constant total energy. In the present work, a matrix of 498 Ar atoms was used. In order to represent the vibrational amplitudes of the Ar atoms we adjusted their velocities to an effective temperature T'. The effective temperature is chosen in such a way that the classical probability distribution for a harmonic oscil-

lator matches the quantum probability distribution in the limit $\hbar \to 0$, and is given by the equation:

$$T' = \frac{\hbar\omega}{2k_B}\left(\tanh\left(\frac{\hbar w}{2k_B T}\right)\right)^{-1} \qquad (4)$$

This way of introducing a quantum correction into the classical treatment was first discussed in ref. 34 and it has been used successfully in molecular dynamics simulations of photodynamic processes of small molecules in the condensed phase.[10,35,36] Using the Debye frequency of solid Ar $\omega = 75$ cm^{-1}, an effective temperature of $T' = 49$ K was required. The equilibration of the system at the desired temperature was performed using the velocity method[37] with a relaxation constant of 0.4 ps. The larger number of Ar atoms avoids box size effects for longer times. 100 trajectories of 30 ps were propagated in order to assure a convergence of the electronic state populations in time.

A. Results

In Fig. 4 we represent the averaged populations of the different electronic states as a function of time. We see a fast decrease of the population initially located in the $^3\Pi_{0+}$ state while the population of the $^1\Pi_1(A'$ and $A'')$ reaches a maximum in the first ps of the photodissociation dynamics. The final efficiency in the population transfer out of $^3\Pi_{0+}$ will be of $\sim 97\%$ after 30 ps of dynamics. Transfer of population to $^1\Pi_1$ can be explained by the passage through the conical intersection several times during this period. Once in the $^1\Pi_1$ state, population can be transferred to the other states that correlate with the $I(^2P_{3/2}) + CN(X\,^2\Sigma^+) + Ar(^1S_0)$ threshold ($^3\Pi_1(A', A'')$ and $X\,^1\Sigma^+$), due to matrix induced coupling near the asymptotic limit.

Fig. 5 shows the total potential energy surfaces (that is, the ICN electronic PES plus the Ar–ICN interaction potential) for the ICN molecule in the $^3\Pi_1$ and $X\,^1\Sigma_{0+}^+$ states. We can see that the Ar matrix creates a potential barrier in both states. In the case of the $^3\Pi_1$ state, it is important to stress that it is dissociative for the free molecule. Its shallow potential minimum is situated far from the absorption Frank–Condon window, so the bound part of this surface cannot be accessed in the gas phase. In the condensed phase it is converted to a bound state due to the effect of the solvent cage.
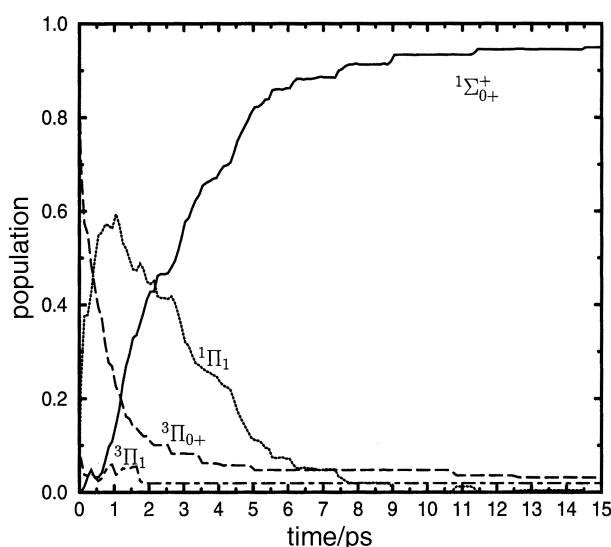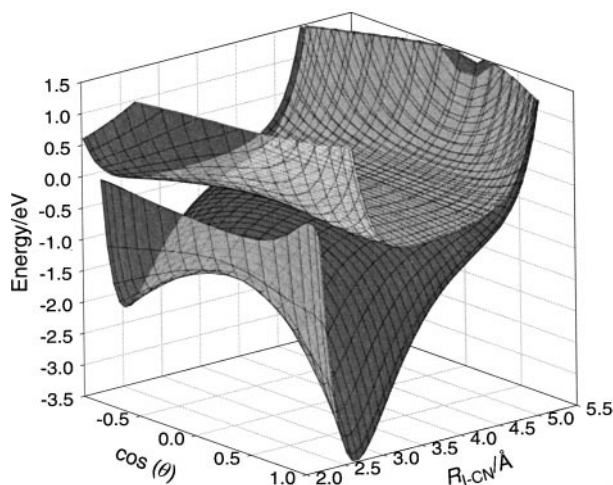
Fig. 5 Potential energy surfaces for the $X\,^1\Sigma_{0+}^+$ and the $^3\Pi_1$ state of ICN in solid Ar as a function of I–CN distance R and bending angle θ. Note the potential barrier induced by the Ar atoms at large I–CN elongations.

Either the $^3\Pi_1$ or the $X\,^1\Sigma^+$ state could stabilise the fragments by relaxing energy sufficiently to trap them. Below a certain vibrational energy, the large internuclear distances (where coupling to other states is important) are no longer accessible. On the other hand, long range interelectronic mixing induced by the solvent can be efficient enough to empty the $^1\Pi_1$ state which loses all its population in less than ~ 15 ps. No population of the $^1\Pi_1$ state was observed after that period. After 30 ps, the final populations of the $^3\Pi_{0+}$, $^1\Pi_1$ and $X\,^1\Sigma^+$ are 3, 2 and 95%, respectively. These values are already attained in the first 15 ps of the photodissociation dynamics and no population changes were observed after that.

Fig. 5 shows that the molecules that recombine and relax in the $^3\Pi_1$ or $X\,^1\Sigma_{0+}^+$ states are either ICN or INC. While only the ICN configuration was observed in the $^3\Pi_1$ state, $\sim 70\%$ of INC was observed in the $X\,^1\Sigma_{0+}^+$ state. This is in good agreement with the experimental estimate for the quantum efficiency of isomerization of 30–70%.[22]

In order to analyse the spatial distribution of ICN molecules at the shallow minimum of the $^3\Pi_1$ state, we have performed hybrid quantum/classical simulations of the system. The Jacobi I–CN distance R and the bending angle θ between $\boldsymbol{R}$ and $\boldsymbol{r}$ were treated quantum mechanically. We have introduced a nuclear wave packet describing the ICN internal coordinates (R, θ) on the $^3\Pi_1$ electronic PES in a matrix of 254 argon atoms. Thus, while the ICN internal coordinates were propagated quantum mechanically in a body fixed frame of the ICN molecule, the other degrees of freedom $(\boldsymbol{Q}(t))$ were propagated classically in the space fixed frame of the matrix.

The wavefunction $\Phi(R, \theta, \boldsymbol{x}, t)$ ($\boldsymbol{x}$ represents the electronic degrees of freedom) that describes the quantum mechanical state at time t is written as:

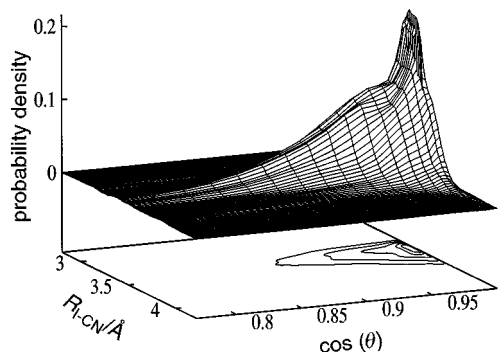$$\Phi(R, \theta, \boldsymbol{x}, t) = \psi(R, \theta, t)\phi(\boldsymbol{x}; R, \theta, \boldsymbol{Q}(t)) \qquad (5)$$

the $\psi(R, \theta, t)$ being nuclear wave packet associated to the electronic wavefunction $\phi(\boldsymbol{x}; R, \theta, \boldsymbol{Q}(t))$ in the $^3\Pi_1$ electronic state. This wave packet is propagated in time by integrating the equations:

$$i\hbar\frac{\partial\psi(R, \theta, t)}{\partial t} = H_q(R, \theta, \boldsymbol{Q}(t))\psi(R, \theta, t) \qquad (6)$$

where

$$H_q(R, \theta, \boldsymbol{Q}(t)) = K_q(R, \theta) + V(R, \theta, \boldsymbol{Q}(t)) \qquad (7)$$

Fig. 4 Average populations of the electronic states treated in the MD-simulations during the first 15 ps after excitation. The population in the $^3\Pi_1$ state remains stable at 2% up to 30 ps.

Fig. 6 Probability density function of a nuclear wavepacket on the $^3\Pi_1$ electronic state of ICN in Ar after 5 ps equilibration to a final temperature of 49 K (classical analogue of 4 K in a quantum mechanical treatment). Population on this electronic surface clearly relaxes to a linear I–CN configuration.

with $K_q(R, \theta)$ being the kinetic energy operator associated to the quantum nuclear coordinates R, θ:

$$K_q(R, \theta) = -\frac{\hbar^2}{2\mu_{I, CN}} \frac{\partial^2}{\partial R^2}$$

$$-\hbar^2\left(\frac{1}{2\mu_{I, CN} R^2} + \frac{1}{2\mu\mu_{CN} r_{eq}^2}\right) \frac{1}{\sin\theta} \frac{\partial}{\partial\theta} \sin\theta \frac{\partial}{\partial\theta} \quad (8)$$

where $\mu_{CN} = m_C m_N/(m_C + m_N)$, $\mu_{I, CN} = m_I(m_C + m_N)/(m_I + m_C + m_N)$ and $V(R, \theta, Q(t))$ the corresponding $^3\Pi_1$ electronic PES.

The classical trajectories are run on the $^3\Pi_1$ electronic state according to Hamilton's equations of motion:

$$\dot{Q} = \left\langle \Phi(t) \left| \frac{\partial H}{\partial P_Q} \right| \Phi(t) \right\rangle$$

$$\dot{P}_Q = -\left\langle \Phi(t) \left| \frac{\partial H}{\partial Q} \right| \Phi(t) \right\rangle \quad (9)$$

where the brackets imply the integration over the electronic (x) and nuclear quantum variables R, θ and $H = H(x, R, \theta, Q)$ is the total Hamiltonian. More details can be found elsewhere.[32]

We have run a hybrid quantum/classical simulation of 5 ps on the $^3\Pi_1$ electronic state. The system was allowed to equilibrate to a final temperature of 49 K. Fig. 6 shows the average probability density function of the nuclear wave packet $\psi(R, \theta, t)$ on the $^3\Pi_1$ electronic state. It is well localised near the ICN linear configuration. This is in agreement with the result obtained with the MDQT trajectories described before. The average R value is ~3.5 Å, *i.e.* almost 1 Å larger than the absorption Franck–Condon region ($R = 2.6$ Å).

Using the nuclear distribution function of Fig. 6 an emission spectrum can be calculated by propagating this ICN wave packet in the electronic ground state and calculating the Fourier transform of the resulting autocorrelation function. The envelope of this spectrum reproduces well the width of the experimental progression (Fig. 1b), but it is blue shifted and the vibrational spacings are smaller than observed. This result is in line with the assignment of the experimental spectra to the $^3\Pi_2$ state, with a similar extended nuclear wave function and a minimum at lower energy and slightly smaller I–CN distance.

IV. Discussion

The combination of experimental data on the near infrared emission due to caged I and CN fragments in the shallow $^3\Pi_2$

potential of ICN, and molecular dynamics simulations allow us to address the issue of population trapping in electronically excited states following the recombination of the I and CN fragments in a condensed phase environment. Indeed, the calculations both support the spectral assignment made in paragraph II B and suggest the mechanisms leading to population trapping in the low lying triplet states.

Fig. 5 illustrates nicely how stable potential wells form in the shallow $^3\Pi_1$ potential due to the presence of the cage. The existence of such cage induced stable wells that can trap population was already suggested in refs. 13 and 14 in order to explain similar infrared emission observed upon UV-excitation of alkyl iodides, but the population mechanism was much simpler in that case due to the absence of efficient excited state non-adiabatic couplings and isomerization. According to Fig. 5 stabilisation in the $^3\Pi_1$ state is equally possible in the INC and in the ICN configuration. However, the experiment and the simulations clearly favour ICN. This preference is probably due to the fact that in the INC configuration the $^3\Pi_1$ state is crossed by the $^1\Pi_1$ surface at a relatively small I–NC distance.[25,28] The latter lies below the $^3\Pi_1$ state at larger distances, and near its potential minimum it crosses the ground state surface. Thus it is very likely that a non-radiative $^3\Pi_1 \rightarrow {}^1\Pi_1 \rightarrow {}^1\Sigma_0^+$ channel empties the $^3\Pi_1$ state in the INC configuration. This provides another argument to rule out INC as a candidate for the near infrared emission.

Since the $^3\Pi_2$ potential is very similar to the $^3\Pi_1$ surface[26] and only slightly lower in energy, we believe that the conclusions drawn for the $^3\Pi_1$ state should not have been very different, had it been included in the simulations. Indeed, just as the $J = 1$ state, it can be populated by non-adiabatic couplings near the asymptotic limit, and in the ICN configuration it can stabilise population at I–CN distances that do not allow non-radiative coupling to the ground state. In any case, in the presence of a nearby, lower lying $^3\Pi_2$ excited state, the population stabilised in $^3\Pi_1$ will probably flow into it on a timescale much shorter than the observed fluorescence decay rate.

Fig. 4 shows that the population stabilises in $^3\Pi_1$ after ~1.8 ps. Within the first 500 fs after excitation the CN fragment undergoes a collision with the cage.[27] Because of the near unity CN to Ar mass ratio, the transfer of energy to the cage is large and there is a significant decrease of CN kinetic energy. Curve crossing to the $^1\Pi_1$ surface occurs at $t \approx 1$ ps, accompanied by a decrease of the I–CN distance beyond ~1.5 ps and a large distribution of ICN angles. This points to the fact that $^3\Pi_1$ is populated upon recombination of I and CN fragments with a large angular distribution. In the INC configuration population flows back to the ground state non-radiatively *via* $^1\Pi_1$, which is lower in energy than the triplet states for large fragment separations, while at smaller angles population gets trapped in the triplet states in a linear ICN configuration and decays radiatively. This is also borne out in Fig. 4: while the $^3\Pi_1$ population has reached a stable level that of the $^3\Pi_{0+}$ and $^1\Pi_1$ is still decreasing, since in the latter two most of the population is in the INC configuration. A population mechanism of lowest lying triplet states by recombination is in line with our thermoluminescence data, where we found that after 'permanent' dissociation of ICN in Ar the near infrared emission occurs in the absence of laser excitation induced by heating of the sample, which results from recombination of I with CN.[22]

The fact that the measured lifetime of the emission in argon is independent of temperature between 4 and 30 K implies that the emitting $^3\Pi_2$ state decays radiatively with unity quantum yield in this matrix. This is reasonable given that $^3\Pi_2$ is the lowest lying excited state and that its minimum is located far away from the ground state potential surface. The decrease in lifetime from Ne to Ar and Kr can therefore not be explained by the occurrence of non-radiative channels. Index

of refraction effects are also too small to account for the important changes. A similar drastic lifetime decrease has been observed in rare gas matrices with unity quantum yield for the $a\,^4\Pi - X\,^2\Pi$ emission of NO (ref. 38) and in the case of the triplet emission of fullerenes.[39] This was qualitatively explained by the fact that a coupling matrix element can arise if both upper and lower impurity states can interact with solvent states that are strongly mixed by spin-orbit coupling.

Finally, we turn to the width of the vibrational structure of the ICN emission bands in the different rare gas matrices. A similar, weakly structured emission as for ICN in Ar and Kr has been observed for the $A\,^3\Pi_{1u} \to X\,^1\Sigma_g^+$ transition of I_2 molecules trapped in solid Kr.[40] In the latter case the width of the vibrational structure could be quantitatively explained by the correlation decay of the surrounding rare gas atoms, which was shown to occur at about the same time as the first recurrence of the intramolecular vibrational wavepacket in the ground state by simulations using a path integral method.[41] Unfortunately, the hybrid quantum/classical technique used for the MD calculations in this work does not allow one to calculate the bath correlation function with the necessary precision. However, just as in the case of iodine, the intramolecular wavepacket in the ground state shows several recurrences in Ar, and only the rare gas contribution can lead to the rapid decorrelation consistent with the measured spectral widths. Since the ground state vibrational frequency is much higher in ICN than in I_2, the correlation decay must be faster in the former, as expected from the larger amplitude of the vibrational motion. In neon no vibrational structure is observed and this is probably due to the fact that the surrounding rare gas atoms are distorted much more strongly by the ~ 1 Å elongation of ICN in the $^3\Pi_2$ state in this tight matrix, and quickly rearrange once the molecule is contracting on the ground state surface. This could also be a reason for the blue shift observed for the near infrared emission in Ne with respect to Ar and Kr.

V. Conclusion

We have presented emission spectra recorded in Ne, Ar and Kr matrices that provide experimental evidence for the stabilisation of caged I and CN fragments in a shallow excited state potential surface in the linear I–CN configuration. Based on a lifetime analysis we identified the emitting state as $^3\Pi_2$, which is the lowest excited state of ICN. The bound part of this state as well as that of the $^3\Pi_1$ state cannot be accessed in the gas phase since they are dissociative and since their shallow wells lie outside the Franck–Condon region for excitation. Stabilisation of population in these states is induced by the matrix, which provides a potential energy barrier to the separation of fragments. This is borne out by calculation of the modified potential surfaces of the ICN molecule in an Ar matrix and by molecular dynamics simulations. They show that indeed $\sim 2\%$ of the total population gets trapped in the $^3\Pi_1$ state in the ICN configuration. The $^3\Pi_1$ state is populated by non-adiabatic couplings induced by the matrix at large I–CN distances, where state mixing becomes significant since several ICN electronic surfaces become quasi-degenerate. If a trajectory remains in the $^3\Pi_1$ state long enough to relax a sufficient amount of its initial kinetic energy, fragments are trapped because the I–CN distance is small enough to make these couplings negligible. On the other hand, no trapping is observed in excited states of the INC configuration, since non-radiative relaxation to the ground state is strongly favoured by the energetics of the isomer.

Even though the simulations do not include the $^3\Pi_2$ surface, we believe that the main conclusions for $^3\Pi_1$ should be valid for both triplet states. Furthermore, population trapped in $^3\Pi_1$ will very probably end up in $^3\Pi_2$ at longer times.

This work stresses the importance of non-adiabatic coupling in condensed phase chemical dynamics. In addition to population trapping due to recombining fragments, cage induced isomerization and permanent cage exit of fragments other competing processes, which are closely intertwined with the one, studied in the present contribution. These processes are discussed in refs. 22, 24, 27, 32 which present a systematic attempt to study a dissociation reaction in the condensed phase of a triatomic molecule in which the diatomic fragment carries away most of the kinetic energy. As such, it serves as the basis for future studies on the effect of caging in liquids using ultrashort pulses and efforts are underway to this aim.

References

1 M. Chergui and N. Schwentner, *Trends Chem. Phys.*, 1992, **2**, 89.
2 V. A. Apkarian and N. Schwentner, *Chem. Rev.*, 1999, **99**, 1481.
3 D. E. Milligan and M. E. Jacox, *J. Chem. Phys.*, 1967, **47**, 278.
4 R. Schriever, M. Chergui, Ö. Ünal, N. Schwentner and V. Stepanenko, *J. Chem. Phys.*, 1990, **93**, 3245.
5 N. Schwentner, M. Chergui, H. Kunz and J. G. McCaffrey, in *Reaction Dynamics in Clusters and Condensed Phases*, Kluwer Academic Publishers, Amsterdam, 1994, p. 521.
6 K.-H. Gödderz, N. Schwentner and M. Chergui, *Chem. Phys.*, 1996, **209**, 91.
7 J. G. McCaffrey, H. Kunz and N. Schwentner, *J. Chem. Phys.*, 1992, **96**, 155.
8 J. Zoval and V. A. Apkarian, *J. Phys. Chem.*, 1994, **98**, 7945.
9 R. Zadoyan, J. Almy and V. A. Apkarian, *Faraday Discuss.*, 1997, **108**, 255.
10 R. Zadoyan, Z. Li, C. C. Martens and V. A. Apkarian, *J. Chem. Phys.*, 1994, **101**, 6648.
11 Q. Liu, J.-K. Wang and A. H. Zewail, *Nature*, 1993, **364**, 427.
12 A. L. Harris, J. K. Brown and C. B. Harris, *Ann. Rev. Phys. Chem.*, 1988, **39**, 341.
13 L. E. Brus and V. E. Bondybey, *Chem. Phys. Lett.*, 1975, **36**, 252.
14 L. E. Brus and V. E. Bondybey, *J. Chem. Phys.*, 1976, **65**, 71.
15 A. V. Benderskii, R. Zadoyan and V. A. Apkarian, *J. Chem. Phys.*, 1997, **107**, 8437.
16 J. C. Tully, *J. Chem. Phys.*, 1990, **93**, 1061.
17 S. Hammes-Schiffer and J. C. Tully, *J. Chem. Phys.*, 1994, **101**, 4657.
18 I. H. Gersonde and H. Gabriel, *J. Chem. Phys.*, 1993, **98**, 2094.
19 V. S. Batista and D. F. Coker, *J. Chem. Phys.*, 1996, **105**, 4033.
20 A. I. Krylov and R. B. Gerber, *J. Chem. Phys.*, 1997, **106**, 6574.
21 Z. Li, J. Y. Fang and C. C. Martens, *J. Chem. Phys.*, 1996, **104**, 6919.
22 J. Helbing and M. Chergui, *J. Phys. Chem.*, in the press.
23 U. Samuni, S. Kahana, R. Fraenkel, Y. Haas, D. Danovich and S. Shaik, *Chem. Phys. Lett.*, 1994, **225**, 391.
24 R. Fraenkel and Y. Haas, *Chem. Phys. Lett.*, 1993, **214**, 234.
25 Y. Amatatsu, S. Yabushita and K. Morokuma, *J. Chem. Phys.*, 1994, **100**, 4894.
26 S. Yabushita and K. Morokuma, *Chem. Phys. Lett.*, 1990, **175**, 518.
27 S. Fernandez-Alberti, N. Halberstadt, J. A. Beswick and J. Echave, *J. Chem. Phys.*, 1998, **109**, 2844.
28 Y. Amatatsu and K. Morokuma, *J. Chem. Phys.*, 1995, **245**, 469.
29 C. H. Becker, P. Casavecchia, Y. T. Lee, R. E. Olso and W. A. Lester Jr, *J. Chem. Phys.*, 1979, **70**, 5477.
30 A. A. Buchachenko and N. F. Stepanov, *J. Chem. Phys.*, 1996, **104**, 9913.
31 Y. Zhao, I. Yourshaw, G. Reiser, C. C. Arnold and D. M. Neumark, *J. Chem. Phys.*, 1994, **101**, 6538.
32 S. Fernandez-Alberti, J. Echave, V. Engel, N. Halberstadt and J. A. Beswick, *J. Chem. Phys.*, 2000, **113**, in the press.
33 M. P. Allen and D. J. Tildesley, in *Computer Simulations of Liquids*, Oxford University Press, Oxford, 1987.

34 J. P. Bergsma, P. H. Berens, K. R. Wilson, D. R. Fredkin and E. J. Heller, *J. Phys. Chem.*, 1984, **88**, 612.

35 C. J. Bardeen, J. Che, K. R. Wilson, V. V. Yakovlev, V. A. Apkarian, C. C. Martens, R. Zadoyan, B. Kohler and M. Messina, *J. Chem. Phys.*, 1997, **106**, 8486.

36 S. Jimenez, A. Pasquarello, R. Car and M. Chergui, *Chem. Phys.*, 1997, **233**, 343.

37 H. J. C. Berendsen, J. P. M. Postma, W. F. van Gunsteren, A. DiNola and J. R. Haak, *J. Chem. Phys.*, 1984, **81**, 3684.

38 F. Vigliotti, G. Zerza, M. Chergui and J. Rubayo-Soneira, *J. Chem. Phys.*, 1998, **109**, 3508.

39 A. Sassara, G. Zerza and M. Chergui, *Chem. Phys. Lett.*, 1996, **261**, 213.

40 M. M. Macler, J.-Ph. Nicolai and M. C. Heaven, *J. Chem. Phys.*, 1989, **91**, 674.

41 M. Ovchinnikov and V. A. Apkarian, *J. Chem. Phys.*, 1996, **105**, 1.